

Array Antenna Power Pattern Analysis Through Quantum Computing

L. Tosi,⁽¹⁾ P. Rocca,⁽¹⁾⁽²⁾ *Senior Member, IEEE*, N. Anselmi,⁽¹⁾ *Member, IEEE*, and A. Massa,⁽¹⁾⁽³⁾⁽⁴⁾ *Fellow, IEEE*

⁽¹⁾ *ELEDIA Research Center (ELEDIA@UNITN - University of Trento)*

Via Mesiano 77, 38123 Trento - Italy

E-mail: {luca.tosi-1, paolo.rocca, nicola.anselmi.1, andrea.massa}@unitn.it

Website: www.eledia.org/eledia-unitn

⁽²⁾ *ELEDIA Research Center (ELEDIA@XIDIAN - Xidian University)*

P.O. Box 191, No.2 South Tabai Road, 710071 Xi'an, Shaanxi Province - China

E-mail: paolo.rocca@xidian.edu.cn

Website: www.eledia.org/eledia-xidian

⁽³⁾ *ELEDIA Research Center (ELEDIA@UESTC - UESTC)*

School of Electronic Engineering, Chengdu 611731 - China

E-mail: andrea.massa@uestc.edu.cn

Website: www.eledia.org/eledia-uestc

⁽⁴⁾ *ELEDIA Research Center (ELEDIA@TSINGHUA - Tsinghua University)*

30 Shuangqing Rd, 100084 Haidian, Beijing - China

E-mail: andrea.massa@tsinghua.edu.cn

Website: www.eledia.org/eledia-tsinghua

This work has been submitted to the IEEE for possible publication. Copyright may be transferred without notice, after which this version may no longer be accessible.

Array Antenna Power Pattern Analysis Through Quantum Computing

L. Tosi, P. Rocca, N. Anselmi, and A. Massa

Abstract

A method for the analysis of the power pattern of phased array antennas (*PA*s) based on the quantum Fourier transform (*QFT*) is proposed. The computation of the power pattern given the set of complex excitations of the *PA* elements is addressed within the quantum computing (*QC*) framework by means of a customized procedure that exploits the quantum mechanics principles and theory. A representative set of numerical results, yielded with a quantum computer emulator, is reported and discussed to assess the reliability of the proposed method by pointing out its features in comparison with the classical approach based on the discrete Fourier transform (*DFT*), as well.

Key words: Array Antenna; Antenna Analysis; Power Pattern; Quantum Computing (*QC*); Quantum Fourier Transform (*QFT*).

1 Introduction

Nowadays, phased array antennas (*PAs*) are a widely adopted technology with countless applications [1][2] such as multiple-input multiple-output (*MIMO*) mobile communications (e.g., 5G) [3]-[5], space communications [6]-[8], automotive [9] and airborne radar systems [10], and weather forecasting [11] as well as biomedical microwave imaging [12][13] or, more in general, non destructive evaluation and testing (*NDE/NDT*) [14]. Indeed, *PAs* stand out for the robustness, the adaptability to conformal surfaces, the easy reconfiguration capabilities, and the careful control of the radiation features [15]. Moreover, it is worth mentioning that unconventional (i.e., clustered [16][17] or thinned/sparse [18][19] architectures) *PAs* are gaining momentum since they are interesting solutions as suitable trade-offs between costs and radiation performance [20].

Typically, the design of *PAs* has been addressed by formulating the synthesis problem at hand as an optimization one, then solved with deterministic [21]-[23] or stochastic [24][25] methods by recurring to machine learning techniques [26], as well. However, a common bottleneck for many design methods is the need of iterating the evaluation of a cost function, which is based on the knowledge/computation of the power pattern, that quantifies the mismatch between synthesized pattern features and the ideal one or against user-defined requirements. Therefore, the computational cost becomes prohibitive in case of large arrays [27] because of the wide dimension of the solution space as well as the huge number of pattern samples to be computed for properly accounting for its angular variations.

The goal of this work is to propose an innovative method, based on *QC*, for the fast computation of the power pattern starting from the array excitations (also indicated as “*PAs analysis*” problem). Indeed, *QC* has the potential for offering a huge computational power, unreachable even by current supercomputers. In the recent years, *QC* has drawn significant attention since it has proved the ability to solve computationally-intensive problems by taking advantage of phenomena exclusively related to the quantum realm. For instance, the superposition and the entanglement have been used in many quantum algorithms to enable a relevant speedup versus classical programs [28]. On the other hand, a widespread use of quantum computers is still prevented by different technical factors such as the high errors intrinsic to the quantum gates

[29], which are used to perform quantum operations, and the instability when dealing with large numbers of quantum bits (qubits) [30]. Despite these technological issues, *QC* has been already exploited in different research branches starting from physics and computational biology [31] up to, more recently, computational electromagnetics [32][33] for the simulation and optimization of complex radiating systems. Undoubtedly, the most well-known applications of *QC* are in the field of information technology as, for instance, quantum machine learning [34] and quantum cryptography [35]. In this latter framework, a very popular *QC* algorithm is the Shor's algorithm [36] that has rendered ineffective the Rivest-Shamir-Adleman (*RSA*) cryptography technique [37] by solving the underlying factoring problem in polynomial time. Moreover, a part of the Shor's algorithm, namely the quantum Fourier transform (*QFT*), has given an exponential advantage in terms of computational efficiency over its classical counterpart [i.e., the discrete Fourier transform (*DFT*)].

In this paper, for the first time to the best of the authors' knowledge, the prediction of the power pattern of *PAs* is efficiently carried out by benefiting of the lower computational costs of the *QFT*. Towards this end, the *PAs analysis problem* is adapted to the quantum domain since, while quantum computers are able to perform all the operations available on classical computers [38], it is mandatory to reformulate the problem at hand to reach the *QC* speedup. More in detail, it means firstly to encode the classical information into the quantum one for taking advantage of the set of *QC* exclusive operations. Moreover, a user of a quantum computer needs to know that the meaning of output data radically differs from the classical one. Indeed, each execution of a quantum program results in the measurement of a quantum state and it is possible to derive the probability of such a state, which is here strictly related to the result of the Fourier transform operation, only by iterating the execution of the program for a number of runs (indicated as '*shots*').

The rest of the paper is organized as follows. In Sect. 2, the *PA* analysis problem is mathematically formulated in the *QC* framework by presenting the *QFT*-based pattern prediction method. Section 3 is devoted to the numerical validation and assessment of the proposed computational approach. Representative numerical results are also provided to give some insights on the behavior of the *QFT* algorithm and the dependence of its performance on the control parameters.

Eventually, some conclusions and final remarks are drawn (Sect. 4).

2 Mathematical Formulation

Let us consider a N elements PA where the array elements are equally-spaced by d along the z -axis (Fig. 1). Each n -th ($n = 0, \dots, N - 1$) element is connected to a transmit-receive module (TRM) that generates a complex excitation w_n , $w_n \triangleq \alpha_n \exp(j\beta_n)$, ($n = 0, \dots, N - 1$), α_n and β_n being the corresponding amplitude and phase, respectively, while $j = \sqrt{-1}$ is the imaginary unit. Let $\underline{g}_n(u)$ be the radiation pattern of the n -th ($n = 0, \dots, N - 1$) array element, then the EM field radiated in far-field (FF) by the PA is given by

$$\underline{F}(u) = \sum_{n=0}^{N-1} w_n \underline{g}_n(u) \exp[j(kdu)n] \quad (1)$$

where $k = 2\pi/\lambda$ is the free-space wavenumber, λ being the corresponding wavelength, and u is the direction cosine ($u \triangleq \cos\theta$), θ ($0 \leq \theta \leq \pi$) being the angle measured from the z -axis. If the array elements are equal [i.e., $\underline{g}_n(u) \simeq \underline{g}(u)$; $n = 0, \dots, N - 1$], the $\underline{F}(u)$ can be written as the product between the element pattern, $\underline{g}(u)$, and the array factor, $A(u)$

$$A(u) \triangleq \sum_{n=0}^{N-1} w_n \exp[j(kdu)n], \quad (2)$$

[i.e., $\underline{F}(u) = \underline{g}(u) A(u)$], and the corresponding power pattern, $P(u)$ ($P(u) \triangleq |\underline{F}(u)|^2$), which mathematically describes the angular distribution of the power either radiated or received by the PA , turns out to be

$$P(u) = |\underline{g}(u)|^2 |A(u)|^2. \quad (3)$$

As it can be observed (3), $P(u)$ directly depends on the absolute square of the array factor, $|A(u)|^2$, and the samples of this latter (2), $\mathbf{A} = \{A_m; m = 0, \dots, M - 1\}$, are related to the set of the array excitations, $\mathbf{w} = \{w_n; n = 0, \dots, N - 1\}$, through the DFT , $\mathbf{A} = DFT(\mathbf{w})$

$$A_m = \sum_{n=0}^{N-1} w_n \exp\left[-j\left(\frac{2\pi}{N}n\right)m\right], \quad m = 0, \dots, M - 1 \quad (4)$$

where $A_m = A(u_m)$ is the m -th ($m = 0, \dots, M - 1$) sample of the array factor (2) at the angular direction $u_m = -m \frac{\lambda}{Nd}$.

Once the discrete sample vector \mathbf{A} has been computed, the corresponding continuous function, $\{A(u); -1 \leq u \leq 1\}$, is obtained by means of a periodic interpolation

$$A(u) = \sum_{m=0}^{M-1} A_m S\left(\pi du + \frac{m\pi}{N}\right), \quad (5)$$

S being the sinc function [$S(x) \triangleq \sin(Nx)/N \sin(x)$].

Under the hypothesis of ideal elements [i.e., $\underline{g}(u) = \underline{1}$] through (3), it turns out that $P(u) = |A(u)|^2$, thus the relation

$$P_m = |A_m|^2 \quad (6)$$

holds true, P_m being the sample of the power patten at $u = u_m$ [i.e., $P_m = P(u_m)$].

The power pattern of the N elements array antenna is then computed in the QC framework with the quantum counterpart of the DFT , namely the QFT . Towards this end, the first step consists in allocating a register of qubits, Ψ , where the input/output values of the Fourier transform are encoded in a set of Q quantum states. More specifically, Ψ is the concatenation of L single qubits, each l -th ($l = 0, \dots, L - 1$) one assuming two possible states, $|\psi_l\rangle \in \{|0\rangle, |1\rangle\}$, and the q -th ($q = 0, \dots, Q - 1$) state of the vector Ψ , $\Psi \leftarrow |\Psi_q\rangle$, is given by the tensor product of each single qubit state $|\Psi_q\rangle = \bigotimes_{l=0}^{L-1} |\psi_l^q\rangle = |\psi_{L-1}^q \dots \psi_l^q \dots \psi_0^q\rangle$. Since a L qubit register, Ψ , can encode at most 2^L different (input/output) states, then a register with $L = \lceil \log_2 Q \rceil$, Q being $Q = \max(N, M)$, qubits must be chosen to yield, through QFT , M samples of the power pattern starting from N array excitations.

The input state vector of the QFT is then initialized by assigning a n -th ($n = 0, \dots, N - 1$) excitation, w_n , to each q -th ($q = 0, \dots, Q - 1$) quantum state, $|\Psi_q\rangle$. More in detail, the first N states of Ψ are assigned to the N -size set of normalized complex excitations $\hat{\mathbf{w}}$, $\hat{\mathbf{w}} \triangleq \left\{ \hat{w}_n \triangleq \frac{w_n}{\|\mathbf{w}\|}; n = 0, \dots, N - 1 \right\}$,⁽¹⁾ while the remaining $Q - N$ ones are set to zero

⁽¹⁾The normalization implies that the sum of the squared modulus of all the weights is unitary (i.e., $\sum_{n=0}^{N-1} |\hat{w}_n|^2 = 1$).

$$|\mathbf{w}\rangle = \sum_{q=0}^{N-1} \hat{w}_q |\Psi_q\rangle + \sum_{q=N}^{Q-1} 0 |\Psi_q\rangle. \quad (7)$$

Analogously to the classical theory, the output state vector $|\mathbf{A}\rangle$

$$|\mathbf{A}\rangle = \sum_{m=0}^{M-1} \hat{A}_m |\Psi_m\rangle \quad (8)$$

is yielded by applying the *QFT* to the input quantum state vector $|\mathbf{w}\rangle$ so that the weight of the state $|\Psi_m\rangle$ ($m = 0, \dots, M - 1$) is given by

$$\hat{A}_m = \frac{1}{\sqrt{M}} \sum_{q=0}^{M-1} \hat{w}_q \exp \left[-j \left(\frac{2\pi}{N} q \right) m \right] |\Psi_q\rangle. \quad (9)$$

Unfortunately, the measurable output of a *QC* operation, as the *QFT* one, is not a variable [e.g., here the complex value of \hat{A}_m ($m = 0, \dots, M - 1$)], but the probability of occurrence of the quantum state associated to it [i.e., $|\Psi_m\rangle$ ($m = 0, \dots, M - 1$)]. On the other hand, the Born rule [38] states that the probability of measuring the m -th ($m = 0, \dots, M - 1$) quantum state, \wp_m , is related to the corresponding m -th weight, \hat{A}_m , as follows

$$\wp_m = \left| \hat{A}_m \right|^2. \quad (10)$$

By comparing (6) and (10), it is easy to infer that

$$\hat{\wp}_m = \hat{P}_m \quad (11)$$

where $\hat{\wp}_m \triangleq \frac{\wp_m}{\wp_{MAX}}$ and $\hat{P}_m \triangleq \frac{P_m}{P_{MAX}}$, \wp_{MAX} and P_{MAX} being the normalization coefficients, $\wp_{MAX} \triangleq \max_{m=0, \dots, M-1} (\wp_m)$ and $P_{MAX} \triangleq \max_{m=0, \dots, M-1} (P_m)$, respectively.

Accordingly, the m -th ($m = 0, \dots, M - 1$) sample of the power pattern of the array, \hat{A}_m , when feeding the array elements with the excitation vector $\hat{\mathbf{w}}$ is directly obtained by setting its value to the probability of occurrence of each m -th ($m = 0, \dots, M - 1$) output vector state, $|\Psi_m\rangle$ (11) without other maths (e.g., the squared modulus) as in the classical *DFT* approach (6).

On the other hand, since the output of a quantum computer is the index of a quantum state, the

probability of measuring the m -th ($m = 0, \dots, M-1$) output quantum state, $|\Psi_m\rangle$, is determined by repeatedly (T being the number of executions or 'shots') running the same program as

$$\wp_m = \frac{V_m}{T} \quad (12)$$

where V_m ($m = 0, \dots, M-1$) is the number of times the m -th state $|\Psi_m\rangle$ has been observed/measured. In a noiseless environment, the value of \wp_m (12) converges to the actual probability when $T \rightarrow \infty$. However, T is a finite number in real cases and it is chosen as a compromise between the computation time and the accuracy of the arising power pattern samples.

3 Numerical Assessment

In this section, the proposed *QFT*-based method for the computation of the power patterns of antenna arrays is assessed by considering various arrays affording different *FF* beam-patterns. For comparison purposes, the power patterns computed with the classical *DFT*-based approach have been set as reference. The *QC* computations have been emulated with the open Python library Qiskit [39] from IBM [40] that faithfully mimics the behavior of a real quantum computer. In all simulations, ideal isotropic antennas have been assumed [i.e., $\underline{g}_n(u) = \underline{g}(u) = \underline{1}$ ($n = 0, \dots, N-1$)] to avoid any bias related to the type of the radiating elements of the array. The first example deals with a linear array of $N = 16$ elements, spaced by $d = \frac{\lambda}{2}$, having real-valued excitations drawn from a Dolph-Chebyshev (*DC*) distribution and affording a power pattern with sidelobe level (*SLL*) equal to $SLL = -15$ [dB]. The power pattern has been computed in $M = 1024$ angular samples, thus $L = 10$ qubits have been allocated for the *QC* process. According to the guidelines in Sect. 2, the complex "amplitudes" of the first N quantum states of $|\mathbf{w}\rangle$ have been initialized with the *DC* excitations in Tab. I, while the others $Q - N = 1008$ entries have been set to zero as indicated by (7). The *QFT* algorithm has been then executed $T = M \times 10^3$ times and the measured quantum state probabilities, $\{\hat{\wp}_m; m = 0, \dots, M-1\}$ being $\wp_{MAX} = 1.418 \times 10^{-2}$, are shown in Fig. 2 along with the reference pattern yielded by interpolating the patter samples from the classical *DFT*. One can

observe that the *QFT* samples almost perfectly fit the *DFT* curve by assessing the reliability of the *QC* pattern-prediction tool.

As for the computational complexity of the proposed analysis method, it is limited to that of the *QFT* and it amounts to $\Delta_Q = \mathcal{O}(\log^2 M)$, while the pattern prediction with the classical *DFT* method needs $\mathcal{O}(M \times \log M)$ and $\mathcal{O}(M)$ operations [i.e., $\Delta_C = \mathcal{O}(M \times (\log M + 1))$] for the fast Fourier transform (*FFT*) and the square of the amplitudes, respectively. Thus, the computational saving thanks to the *QC* turns out to be $\frac{\Delta_C}{\Delta_Q} > \frac{M}{\log M}$.

Figure 2 also shows that the samples of the *QFT* are always above a minimum 'resolution' threshold δ defined as

$$\delta = \frac{1}{V_{MAX}} \quad (13)$$

where V_{MAX} is the maximum number of times the most recurring output quantum state has been measured (i.e., $V_{MAX} \triangleq \arg \{\max_m (V_m)\}$). In this case, $\delta = -41.6$ [dB] being $V_{MAX} = 1.4518 \times 10^2$.

Since V_{MAX} is expected to statistically grow with T , the value of the resolution threshold δ should get smaller and smaller (i.e., samples with lower amplitudes can be observed) when more shots are used for the quantum computation. To assess such a relation between T and δ , the *QFT* pattern prediction has been performed by varying T , while keeping the same *DC* input state vector, $|\mathbf{w}\rangle$, of the previous example. In particular, the $M = 1024$ pattern samples in Fig. 3 have been computed using $T = M \times 8$ [Fig. 3(a)], $T = M \times 20$ [Fig. 3(b)], $T = M \times 40$ [Fig. 3(c)], and $T = M \times 80$ [Fig. 3(d)] shots and the smallest representable values of the power patterns turn out to be equal to $\delta = -21.5$ [dB], $\delta = -25.0$ [dB], $\delta = -27.8$ [dB], and $\delta = -30.9$ [dB], respectively. Moreover, to provide a statistically reliable assessment, each simulation has been repeated $R = 20$ times and Figure 4 shows the behavior of the average (solid line) value of δ along with its minimum and maximum bounds (shaded region). As expected, the plot confirms the monotonic decreasing dependence of δ on T .

In the third numerical experiment, the dependence of the accuracy of the *QFT*-based analysis method on the *SLL* of the reference pattern has been evaluated still considering the $N = 16$ $d = \frac{\lambda}{2}$ -spaced array, but with the excitations in Tab. I affording the three *DC* patterns having $SLL = \{-15, -20, -25\}$ [dB]. Figure 5 summarizes the outcomes of the *QFT* prediction

process ($M = 1024$ and $L = 10$) when applied to the $SLL = -20$ [dB] and the $SLL = -25$ [dB] cases by setting $T = M \times 80$ shots as in Fig. 3(d) ($SLL = -15$ [dB]). From the comparison, it turns out that there is a growing number of misplaced samples around the sidelobe peaks when lowering the SLL from $SLL = -15$ [dB] [Fig. 3(d)] down to $SLL = -25$ [dB] [Fig. 5(b)] since the prediction of the samples with smaller power pattern values needs more and more shots ($T \uparrow$) as pointed out by the analysis in Fig. 3.

To quantify the mismatch between the reference *DFT* pattern and the *QFT* one, the following (average) pattern matching metric

$$\Gamma \triangleq \frac{1}{R} \sum_{r=1}^R \frac{\sum_{m=0}^{M-1} |\hat{P}_m - \hat{\phi}_m^{(r)}|}{\sum_{m=0}^{M-1} \hat{P}_m} \quad (14)$$

has been used, $\hat{\phi}_m^{(r)}$ being the normalized probability of measuring the m -th ($m = 0, \dots, M-1$) output quantum states at the r -th ($1 \leq r \leq R$) run of the *QC* process. While one should expected a more faithful pattern matching for higher SLL (Fig. 5), the behavior of the plots in Fig. 6 proves the opposite since the Γ value gets worse as SLL increases. Such an (apparently) contradictory outcome can be explained by separately analyzing the mainlobe (*ML*)

$$\Gamma_{ML} = \frac{1}{R} \sum_{r=1}^R \frac{\sum_{m=\chi_1+1}^{\chi_2-1} |\hat{P}_m - \hat{\phi}_m^{(r)}|}{\sum_{m=0}^{M-1} \hat{P}_m} \quad (15)$$

and the sidelobe (*SL*)

$$\Gamma_{SL} = \frac{1}{R} \sum_{r=1}^R \frac{\sum_{m=-1}^{\chi_1} |\hat{P}_m - \hat{\phi}_m^{(r)}| + \sum_{m=\chi_2}^1 |\hat{P}_m - \hat{\phi}_m^{(r)}|}{\sum_{m=0}^{M-1} \hat{P}_m} \quad (16)$$

contributions to the pattern matching metric (14), χ_1 and χ_2 ($\chi_1, \chi_2 \in [0, M-1]$) being the indexes of the pattern samples in the angular positions closer to the nulls on the left and right of the mainlobe, respectively, while the same normalization factor of (14) has been kept to fulfil the condition $\Gamma = \Gamma_{ML} + \Gamma_{SL}$.

The dashed-line plots of Γ_{ML} and Γ_{SL} in Fig. 6 indicate that the mismatch is mainly in the *SL* region (i.e., $\Gamma_{SL} > \Gamma_{ML}$) and the Γ_{SL} value is greater when the SLL of the reference pat-

tern reduces (i.e., $\Gamma_{SL}|_{SLL=-25\text{ [dB]}} > \Gamma_{SL}|_{SLL=-20\text{ [dB]}} > \Gamma_{SL}|_{SLL=-15\text{ [dB]}}$) according to the conclusions drawn from Fig. 3(b) and Figs. 5(a)-5(b). Otherwise, the mainlobe index, Γ_{ML} , decreases (i.e., $\Gamma_{ML}|_{SLL=-25\text{ [dB]}} < \Gamma_{ML}|_{SLL=-20\text{ [dB]}} < \Gamma_{ML}|_{SLL=-15\text{ [dB]}}$) and it is almost constant for smaller SLL values independently on T (e.g., see Γ_{ML} vs. T when $SLL = -25$ [dB] - Fig. 6). Such a behavior strictly depends on the fact that a fixed number of pattern samples, M , is used for the QFT computation and the number of samples entering in the mainlobe, which is proportional to the so-called first-null beam width ($FNBW$), grows when lowering the SLL . Therefore, patterns with wider $FNBW$ (\rightarrow lower SLL) involve more 'high-probability' quantum states over the total number M and, since such states are more carefully predicted (even with few shots) being the most probable, it turns out that the QFT performance (i.e., the total pattern matching error, Γ) improve.

However, one is usually more interested in characterizing the pattern as a whole, thus having sufficient details of the least probable states (i.e., the low pattern values), as well. To infer the optimal trade-off T , so that an accurate matching of the reference power pattern regardless of its SLL is yielded, the Γ_{SL} value of the pattern in Fig. 2 (i.e., $\Gamma_{SL}^{th} = 5.8 \times 10^{-2}$) has been set as quality-target threshold and the QFT simulations have been run by progressively increasing the number of shots T until the condition $\Gamma_{SL}(T) \leq \Gamma_{SL}^{th}$ has hold true. The accuracy threshold Γ_{SL}^{th} has been reached after $T|_{SLL=-20\text{ [dB]}} = 1.8 \times M \times 10^3$ and $T|_{SLL=-25\text{ [dB]}} = 2.4 \times M \times 10^3$ shots, respectively (Fig. 7). Figure 8 shows the corresponding QFT results when predicting the reference DC pattern with $SLL = -20$ [dB] [Fig. 8(a)] and $SLL = -25$ [dB] [Fig. 8(b)]. As expected, there is a more faithful fitting of the reference pattern in the whole angular range and, in particular, within the sidelobe regions [e.g., Fig. 8(a) vs. Fig. 5(a) and Fig. 8(b) vs. Fig. 5(b)].

While previous examples dealt with reference patterns with equi-ripple sidelobes from DC distributions, the performance of the QC -based method have been assessed next for a $d = \frac{\lambda}{2}$ -spaced array with the $N = 16$ Taylor excitations in Tab. I affording a power pattern with decreasing sidelobe peaks when moving far from the mainlobe (i.e., $SLL=-15$ [dB] and $\bar{n} = 4$). The QFT process has been applied by varying the number of shots from $T = M \times 2$ up to $T = M \times 10^3$ and repeating each test $R = 20$ times. The behavior of the pattern matching indexes is shown

in Fig. 9(a) and, as a representative example, Figure 9(b) gives the *QFT* power pattern characterized by $\Gamma_{SL} = \Gamma_{SL}^{th} (\Rightarrow T = M \times 10^3 \text{ shots})$ to prove that it is possible to compute a generic pattern with the required degree of accuracy subject to a proper choice of the number T of *QC* shots.

The last example is concerned with the shaped beam patterns generated by the complex sets of excitations in Fig. 10. For both the flat-top and the cosecant-square patterns, the results in Fig. 11 indicate that the main deviations from the reference pattern occur in the *SL* region (i.e., $\Gamma_{SL} > \Gamma_{ML}$) whatever the T value, despite the main lobe occupies a non-negligible part of the whole visible range $-1 \leq u \leq 1$. Once again the reason is that the quantum states associated to the samples in the *ML* region (i.e., the samples of the power pattern with higher magnitudes) have higher probability of being observed in the measurements also for low values of T (e.g., $T = M \times 10$) [Figs. 12(a)-12(b)], while the *SL* region is better predicted when T grows to $T = M \times 10^2$ [Figs. 12(c)-12(d)] and $T = M \times 10^3$ [Figs. 12(e)-12(f)].

4 Conclusions

An innovative *QC*-based method for the analysis of the power pattern of array antennas has been proposed. It exploits the *QFT* algorithm to yield a suitable accuracy in the pattern prediction with a significant improvement of the computational efficiency with respect to classical *DFT*-based analysis technique. A representative set of numerical examples has been reported and discussed to provide in depth observations on the behaviour and the performance of the proposed method.

To the best of the authors' knowledge, the main innovative contributions of this paper with respect to the state-of-the-art lie in

- the formulation of the *PA* analysis problem in the *QC* framework;
- the adaptation of the *QFT* algorithm for the computation of the *PA* power pattern and the exploitation of the relationship between the probability values of the output quantum states and the samples of the power pattern;

- the exploitation of the quantum parallelism to yield an exponential acceleration in the computation of the power pattern with respect to the classical *DFT* method;
- the study of the dependence of the pattern prediction accuracy of the proposed *QC*-based method on the number of shots/observations to give to the interested readers some useful guidelines to yield a reliable and effective prediction of the power pattern on the basis of the user needs.

Future works, beyond the scope of this paper, will be devoted to implement hybrid algorithms where only computationally-intensive tasks are delegated to a quantum computer, while leaving other data processing operations to a classical computer.

Acknowledgements

This work benefited from the networking activities carried out within the Project CYBER-PHYSICAL ELECTROMAGNETIC VISION: Context-Aware Electromagnetic Sensing and Smart Reaction (EMvisioning) (Grant no. 2017HZJXSZ) funded by the Italian Ministry of Education, University, and Research under the PRIN2017 Program (CUP: E64I19002530001). Moreover, it benefited from the networking activities carried out within the Project SPEED (Grant No. 61721001) funded by National Science Foundation of China under the Chang-Jiang Visiting Professorship Program, the Project 'Inversion Design Method of Structural Factors of Conformal Load-bearing Antenna Structure based on Desired EM Performance Interval' (Grant no. 2017HZJXSZ) funded by the National Natural Science Foundation of China, and the Project 'Research on Uncertainty Factors and Propagation Mechanism of Conformal Load-bearing Antenna Structure' (Grant No. 2021JZD-003) funded by the Department of Science and Technology of Shaanxi Province within the Program Natural Science Basic Research Plan in Shaanxi Province. A. Massa wishes to thank E. Vico for her never-ending inspiration, support, guidance, and help.

References

- [1] R. J. Mailloux, *Phased array antenna handbook* (3rd Ed.). Boston, MA, USA: Artech House, 2018.
- [2] R. L. Haupt, *Antenna arrays - A computation approach*. Hoboken, NJ, USA: Wiley, 2010.
- [3] G. Yang and S. Zhang, "Dual polarized wide-angle scanning phased array antenna for 5G communication system," *IEEE Trans. Antennas Propag.*, DOI: 10.1109/TAP.2022.3141188.
- [4] J. Park, H. Seong, Y. N. Whang, and W. Hong, "Energy-efficient 5G phased arrays incorporating vertically polarized endfire planar folded slot antenna for mmWave mobile terminals," *IEEE Trans. Antennas Propag.*, vol. 68, no. 1, pp. 230-241, Jan. 2020.
- [5] A. Puglielli, A. Townley, G. LaCaille, V. Milovanovic, P. Lu, K. Trotskovsky, A. Whitcombe, N. Narevsky, G. Wright, T. Courtade, E. Alon, B. Nikolic, and A. M. Niknejad, "Design of energy- and cost-efficient massive MIMO arrays," *Proc. IEEE*, vol. 104, no. 3, pp. 586-606, Mar. 2016.
- [6] F. Davarian, "Uplink arrays for the deep space network," *Proc. IEEE*, vol. 95, no. 10, pp. 1923-1930, Oct. 2007.
- [7] R. Schulze, R. E. Wallis, R. K. Stilwell, and W. Cheng, "Enabling antenna systems for extreme deep-space mission applications," *Proc. IEEE*, vol. 95, no. 10, pp. 1976-1985, Oct. 2007.
- [8] S. -M. Moon, S. Yun, I. -B. Yom, and H. L. Lee, "Phased array shaped-beam satellite antenna with boosted-beam control," *IEEE Trans. Antennas Propag.*, vol. 67, no. 12, pp. 7633-7636, Dec. 2019.
- [9] T. Yu and G. M. Rebeiz, "A 22-24 GHz 4-element CMOS phased array with on-chip coupling characterization," *IEEE J. Solid-State Circuits*, vol. 43, no. 9, pp. 2134-2143, Sep. 2008.

- [10] G. Gottardi, L. Poli, P. Rocca, A. Montanari, A. Aprile, and A. Massa, "Optimal monopulse beamforming for side-looking airborne radars," *IEEE Antennas Wireless Propag. Lett.*, vol. 16, pp. 1221-1224, 2017.
- [11] Z. Li, Y. Zhang, L. Borowska, I. R. Ivic, D. Mirkovic, S. Perera, G. Zhang, and D. S. Zrnic, "Polarimetric phased array weather radar data quality evaluation through combined analysis, simulation, and measurements," *IEEE Geosci. Remote Sens. Lett.*, vol. 18, no. 6, pp. 1029-1033, Jun. 2021.
- [12] O. M. Bucci, L. Crocco, R. Scapaticci, and G. Bellizzi, "On the design of phased arrays for medical applications," *Proc. IEEE*, vol. 104, no. 3, pp. 633-648, Mar. 2016.
- [13] F. Tofigh, J. Nourinia, M. Azarmanesh, and K. M. Khazaei, "Near-field Focused array microstrip planar antenna for medical applications," *IEEE Antennas Wireless Propag. Lett.*, vol. 13, pp. 951-954, 2014.
- [14] P.-F. Li, S.-W. Qu, and S. Yang, "Two-dimensional imaging based on near-field focused array antenna," *IEEE Antennas Wireless Propag. Lett.*, vol. 18, no. 2, pp. 274-278, Feb. 2019.
- [15] J. S. Herd and M. D. Conway, "The evolution to modern phased array architectures," *Proc. IEEE*, vol. 104, no. 3, pp. 519-529, Mar. 2016.
- [16] A. Benoni, P. Rocca, N. Anselmi, and A. Massa, "Hilbert-ordering based clustering of complex-excitations linear arrays," *IEEE Trans. Antennas Propag.*, DOI: 10.1109/TAP.2022.3164161.
- [17] P. Rocca, L. Poli, N. Anselmi, and A. Massa, "Nested optimization for the synthesis of asymmetric shaped beam patterns in subarrayed linear antenna arrays," *IEEE Trans. Antennas Propag.*, vol. 70, no. 5, pp. 3385-3397, May 2022.
- [18] G. Oliveri, M. Donelli, and A. Massa, "Linear array thinning exploiting almost difference sets," *IEEE Trans. Antennas Propag.*, vol. 57, no. 12, pp. 3800-3812, Dec. 2009.

- [19] L. Poli, P. Rocca, M. Salucci, and A. Massa, "Reconfigurable thinning for the adaptive control of linear arrays," *IEEE Trans. Antennas Propag.*, vol. 61, no. 10, pp. 5068-5077, Oct. 2013.
- [20] P. Rocca, G. Oliveri, R. J. Mailloux, and A. Massa, "Unconventional phased array architectures and design methodologies - a review," *Proc. IEEE*, vol. 104, no. 3, pp. 544-560, Mar. 2016.
- [21] P. Rocca, N. Anselmi, and A. Massa, "Optimal synthesis of robust beamformer weights exploiting interval analysis and convex optimization," *IEEE Trans. Antennas Propag.*, vol. 62, no. 7, pp. 3603-3612, Jul. 2014.
- [22] B. Fuchs, "Synthesis of sparse arrays with focused or shaped beampattern via sequential convex optimizations," *IEEE Trans. Antennas Propag.*, vol. 60, no. 7, pp. 3499-3503, Jul. 2012.
- [23] M. Yilmaz, N. R. Dhansri, and N. Yilmazer, "Convex beam synthesis for system-oriented noisy and optimal antenna arrays," *IEEE Antennas Wireless Propag. Lett.*, vol. 16, pp. 509-512, 2017.
- [24] C. Lin, A. Qing, and Q. Feng, "Synthesis of unequally spaced antenna arrays by using differential evolution," *IEEE Trans. Antennas Propag.*, vol. 58, no. 8, pp. 2553-2561, Aug. 2010.
- [25] P. Angeletti, L. Berretti, S. Maddio, G. Pelosi, S. Selleri, and G. Toso, "Phase-only synthesis for large planar arrays via Zernike polynomials and invasive weed optimization," *IEEE Trans. Antennas Propag.*, vol. 70, no. 3, pp. 1954-1964, Mar. 2022.
- [26] C. Cui, W. T. Li, X. T. Ye, Y. Q. Hei, P. Rocca, and X. W. Shi, "Synthesis of mask-constrained pattern-reconfigurable nonuniformly spaced linear arrays using artificial neural networks," *IEEE Trans. Antennas Propag.*, vol. 70, no. 6, pp. 4355-4368, Jun. 2022.
- [27] P. Rocca, M. D'Urso, and L. Poli, "Advanced strategy for large antenna array design with subarray-only amplitude and phase control," *IEEE Antennas Wireless Propag. Lett.*, vol. 13, pp. 91-94, 2014.

- [28] D. Deutsch and R. Josza, “Rapid solution of problems by quantum computation,” *Proc. Math. Phys. Eng. Sci.*, vol. 439, no. 1907, pp. 553-558, 1992.
- [29] M. Nielsen and I. Chuang, *Quantum Computation and Quantum Information*. Cambridge, MA, USA: Cambridge University Press, 2000.
- [30] M. M. Wilde, *Quantum Information Theory* (2nd Ed.). Cambridge, UK: Cambridge University Press, 2017.
- [31] S. McArdle, S. Endo, A. Aspuru-Guzik, S. C. Benjamin, and X. Yuan, “Quantum computational chemistry,” *Rev. Mod. Phys.*, vol.92, pp. 015003, Mar. 2020.
- [32] P. Rocca, N. Anselmi, G. Oliveri, A. Polo, and A. Massa, “Antenna array thinning through quantum Fourier transform,” *IEEE Access*, vol. 9, pp. 124313-124323, 2021.
- [33] C. Ross, G. Gradoni, Q. J. Lim, and Z. Peng, “Engineering reflective metasurfaces with ising hamiltonian and quantum annealing,” *IEEE Trans. Antennas Propag.*, vol. 70, no. 4, pp. 2841-2854, Apr. 2022.
- [34] M. Schuld, A. Bocharov, K. M. Svore, and N. Wiebe, “Circuit-centric quantum classifiers,” *Phys. Rev.*, Vol. 101, pp. 032308 Mar. 2020.
- [35] F. Xu, M. Curty, B. Qi, and H. Lo, “Measurement-device-independent quantum cryptography,” *IEEE J. Sel. Topics Quantum Electron.*, vol. 21, no. 3, pp. 148-158, May-Jun. 2015.
- [36] P. W. Shor, “Polynomial-time algorithms for prime factorization and discrete logarithms on a quantum computer,” *SIAM J. Comput.*, vol. 26, no. 11, pp. 303-332, 1999.
- [37] R. Rivest, A. Shamir, and L. Adleman, “A method for obtaining digital signatures and public-key cryptosystems,” *Commun. ACM*, vol. 21, no. 2, pp. 120-126, 1978.
- [38] E. Rieffel and W. Polak, *Quantum computing*. Cambridge, Massachusetts: MIT Press, 2014.

- [39] G. Aleksandrowicz et *al.*, “Qiskit: An open-source framework for quantum computing,” *Zenodo*, Jan. 2019. [Online]. Available: <https://doi.org/10.5281/zenodo.2562111>.
- [40] IBM Quantum. Available: <https://quantum-computing.ibm.com>.

FIGURE CAPTIONS

- **Figure 1.** Sketch of the array architecture
- **Figure 2.** *Numerical Assessment* ($N = 16$, $d = \frac{\lambda}{2}$, *DC* excitations, $SLL = -15$ [dB], $M = 1024$, $T = M \times 10^3$) - Power patterns and resolution threshold.
- **Figure 3.** *Numerical Assessment* ($N = 16$, $d = \frac{\lambda}{2}$, *DC* excitations, $SLL = -15$ [dB], $M = 1024$) - Power patterns and resolution threshold when (a) $T = M \times 8$, (b) $T = M \times 20$, (c) $T = M \times 40$, and (d) $T = M \times 80$.
- **Figure 4.** *Numerical Assessment* ($N = 16$, $d = \frac{\lambda}{2}$, *DC* excitations, $SLL = -15$ [dB], $M = 1024$) - Behavior of the *QFT* resolution threshold statistics versus the number of shots T [average value - (solid line) and interval values within the upper/lower bounds (shaded region)].
- **Figure 5.** *Numerical Assessment* ($N = 16$, $d = \frac{\lambda}{2}$, *DC* excitations, $M = 1024$, $T = M \times 80$) - Power patterns when (a) $SLL = -20$ [dB] and (b) $SLL = -25$ [dB].
- **Figure 6.** *Numerical Assessment* ($N = 16$, $d = \frac{\lambda}{2}$, *DC* excitations, $M = 1024$) - Behavior of the pattern matching metrics versus the number of shots T .
- **Figure 7.** *Numerical Assessment* ($N = 16$, $d = \frac{\lambda}{2}$, *DC* excitations, $M = 1024$) - Behaviour of the *SL* contribution of the pattern matching error, Γ_{SL} , versus the number of shots T .
- **Figure 8.** *Numerical Assessment* ($N = 16$, $d = \frac{\lambda}{2}$, *DC* excitations, $M = 1024$) - Power patterns when (a) $SLL = -20$ [dB] and $T = 1.8 \times 10^3 \times M$ and (b) $SLL = -25$ [dB] and $T = 2.4 \times 10^3 \times M$.
- **Figure 9.** *Numerical Assessment* ($N = 16$, $d = \frac{\lambda}{2}$, *Taylor* excitations, $M = 1024$) - Plots of (a) pattern matching metrics versus the number of shots T and (b) power pattern when $T = M \times 10^3$.
- **Figure 10.** *Numerical Assessment* ($N = 16$, $d = \frac{\lambda}{2}$) - Normalized excitations of the array elements.

- **Figure 11.** *Numerical Assessment* ($N = 16, M = 1024$) - Behavior of the pattern matching metrics versus the number of shots T .
- **Figure 12.** *Numerical Assessment* ($N = 16, M = 1024$) - Plots of the power patterns of the (a)(c)(e) flat-top and (b)(d)(f) cosecant-square beams when (a)(b) $T = M \times 10$, (c)(d) $T = M \times 10^2$, and (e)(f) $T = M \times 10^3$.

TABLE CAPTIONS

- **Table I.** *Numerical Assessment* ($N = 16, d = \frac{\lambda}{2}$) - Normalized excitations.

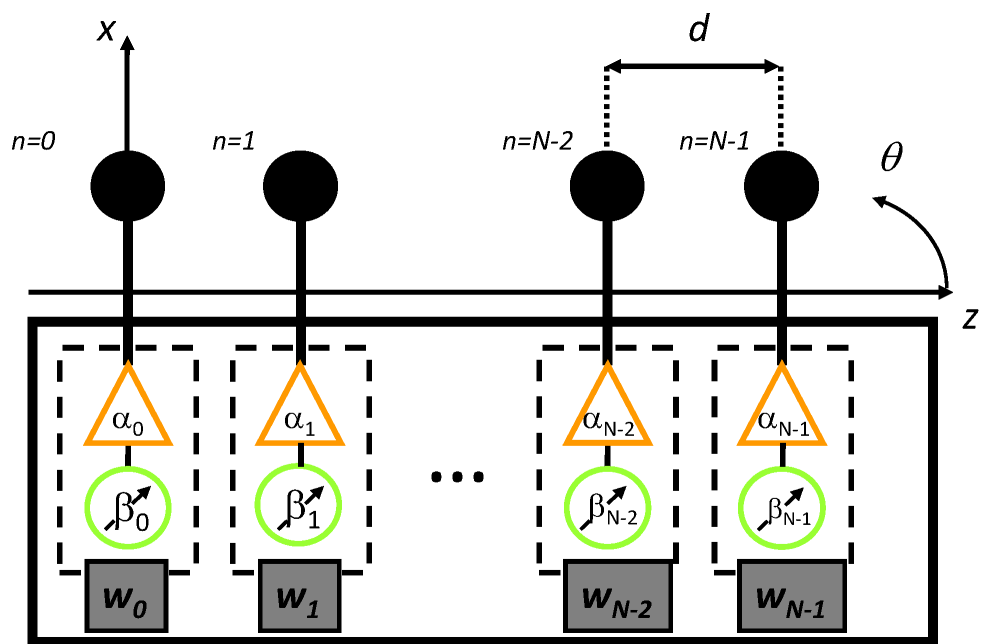


Fig. 1 - L. Tosi et *al.*, “Array Antenna Power Pattern Analysis ...”

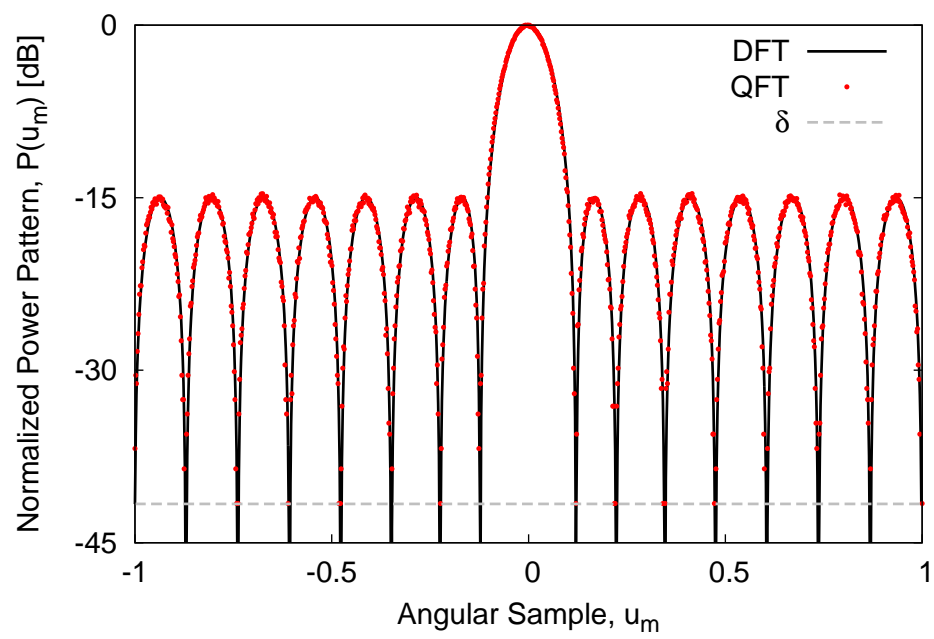
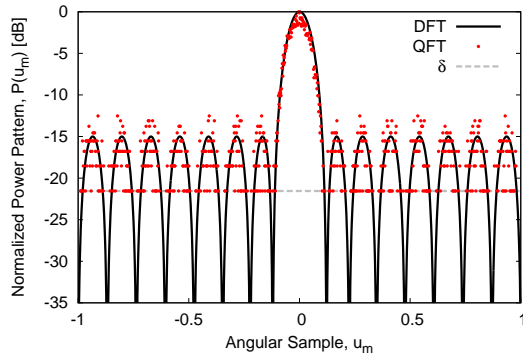
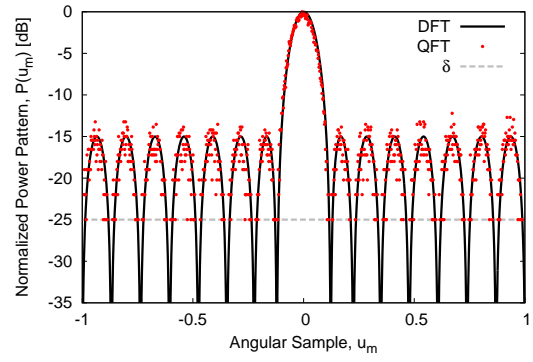


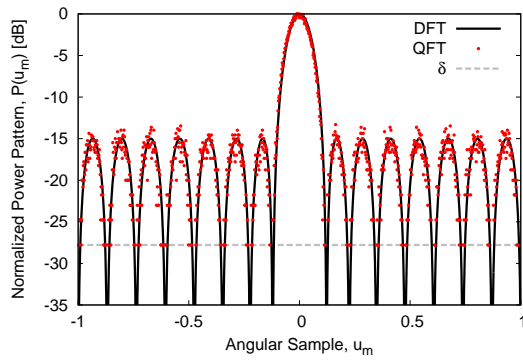
Fig. 2 - L. Tosi et al., “Array Antenna Power Pattern Analysis ...”



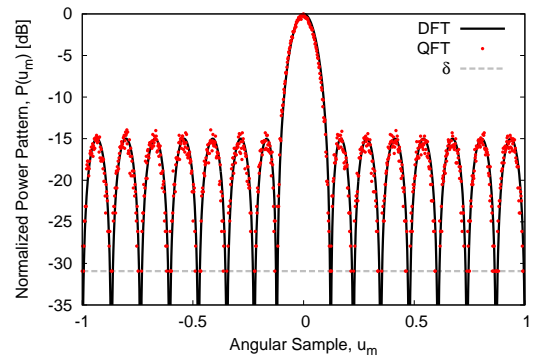
(a)



(b)



(c)



(d)

Fig. 3 - L. Tosi et al., “Array Antenna Power Pattern Analysis ...”

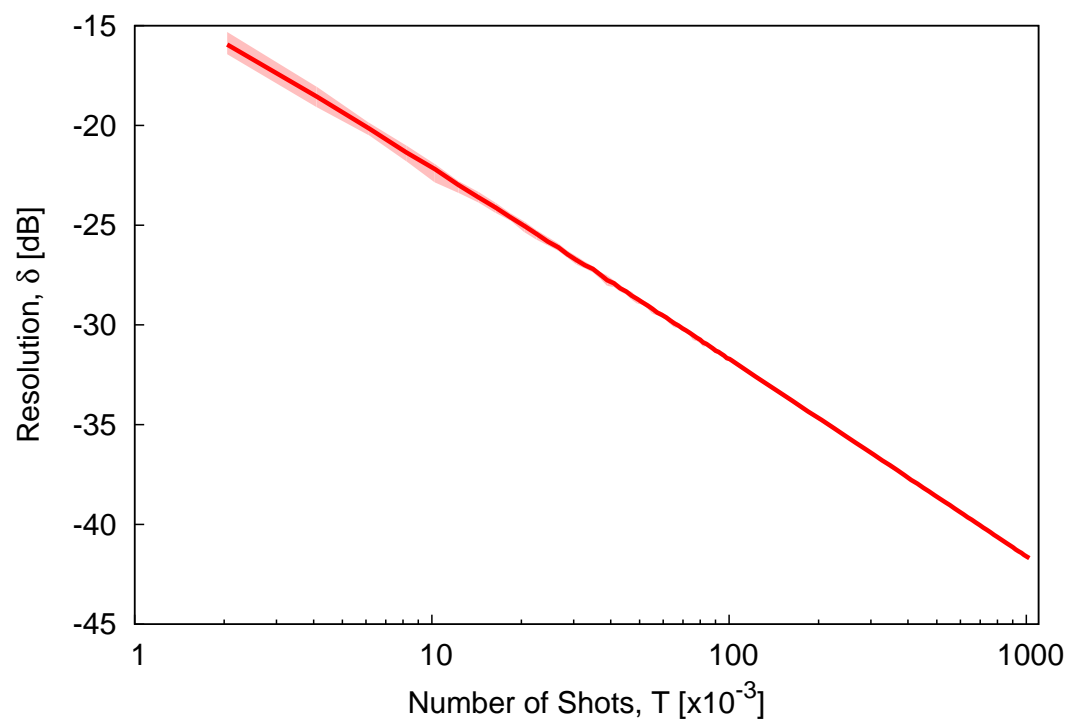
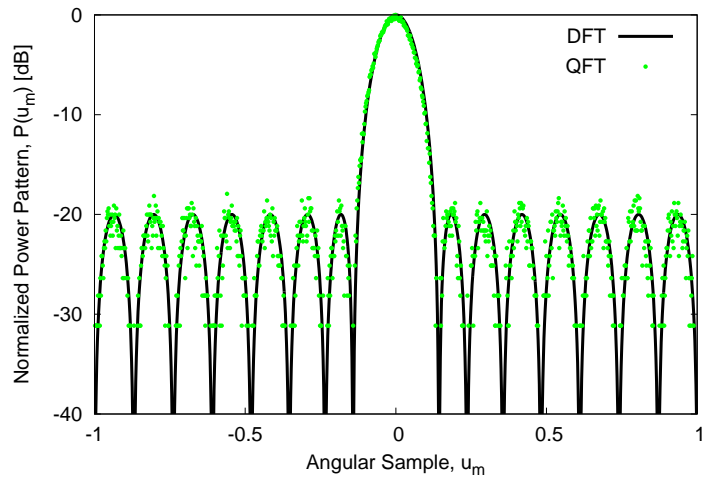
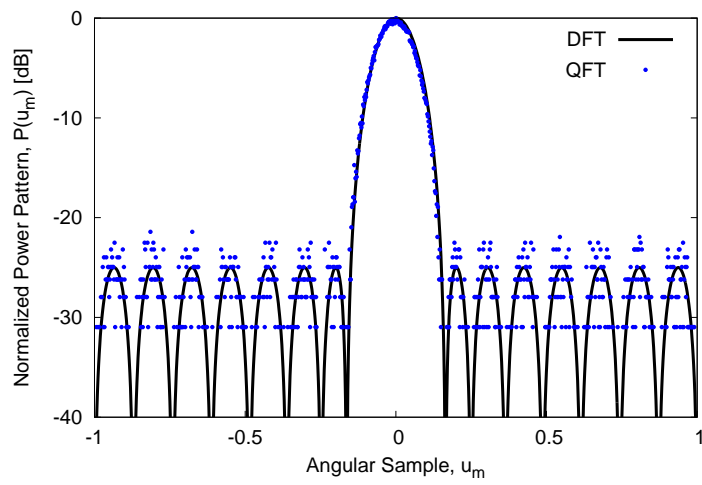


Fig. 4 - L. Tosi et al., “Array Antenna Power Pattern Analysis ...”



(a)



(b)

Fig. 5 - L. Tosi et al., “Array Antenna Power Pattern Analysis ...”

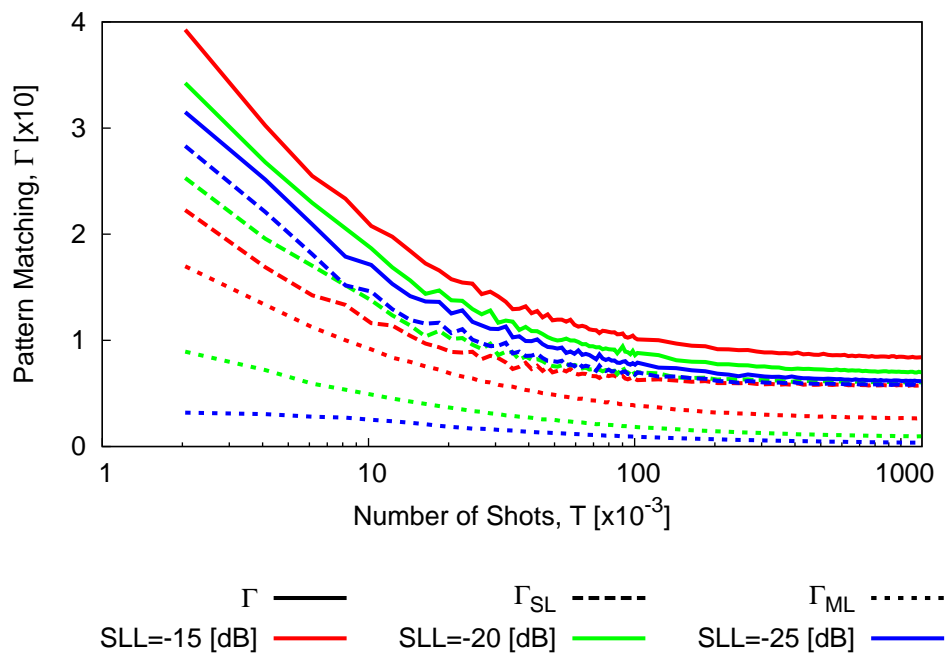


Fig. 6 - L. Tosi et al., “Array Antenna Power Pattern Analysis ...”

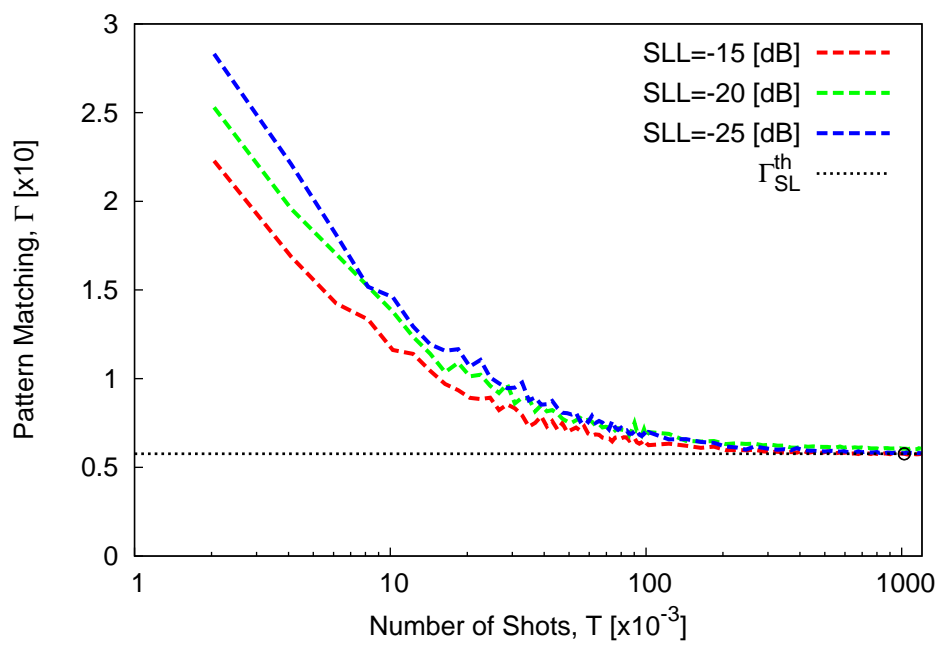
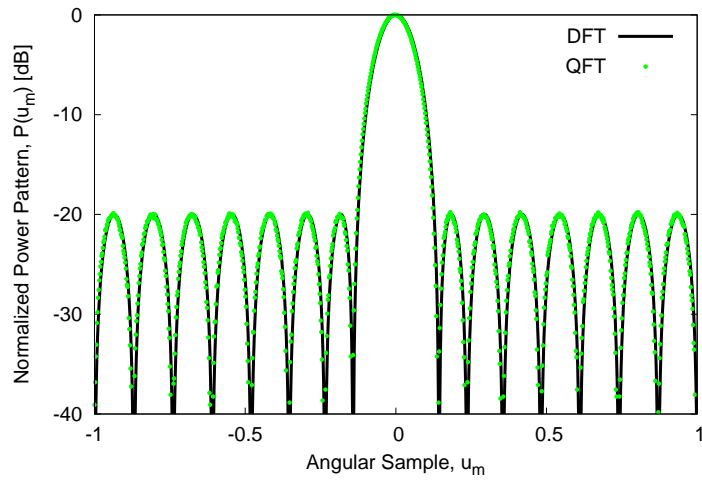
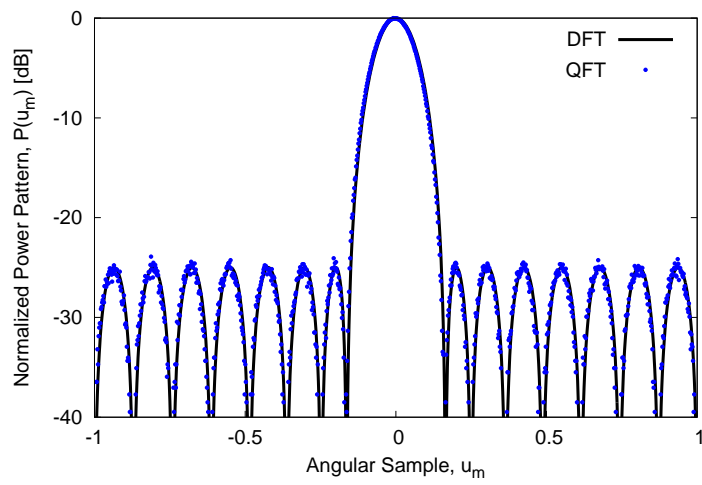


Fig. 7 - L. Tosi et al., “Array Antenna Power Pattern Analysis ...”

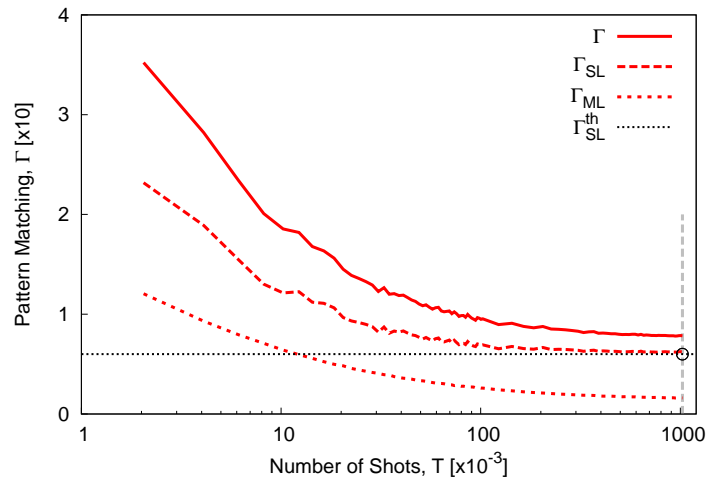


(a)

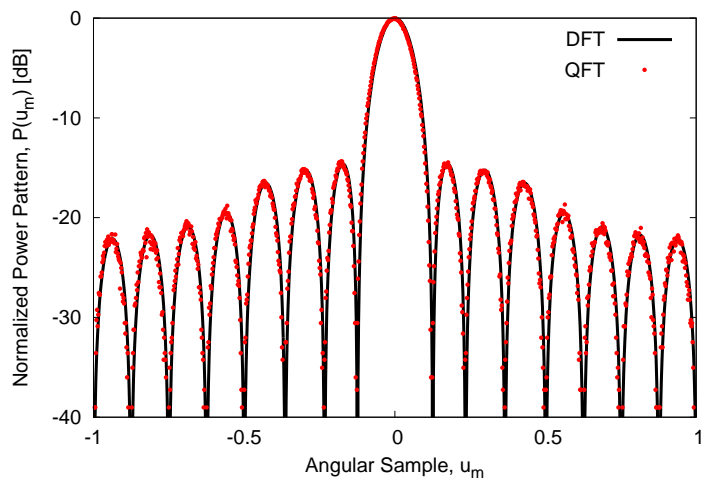


(b)

Fig. 8 - L. Tosi et al., “Array Antenna Power Pattern Analysis ...”



(a)



(b)

Fig. 9 - L. Tosi et al., “Array Antenna Power Pattern Analysis ...”

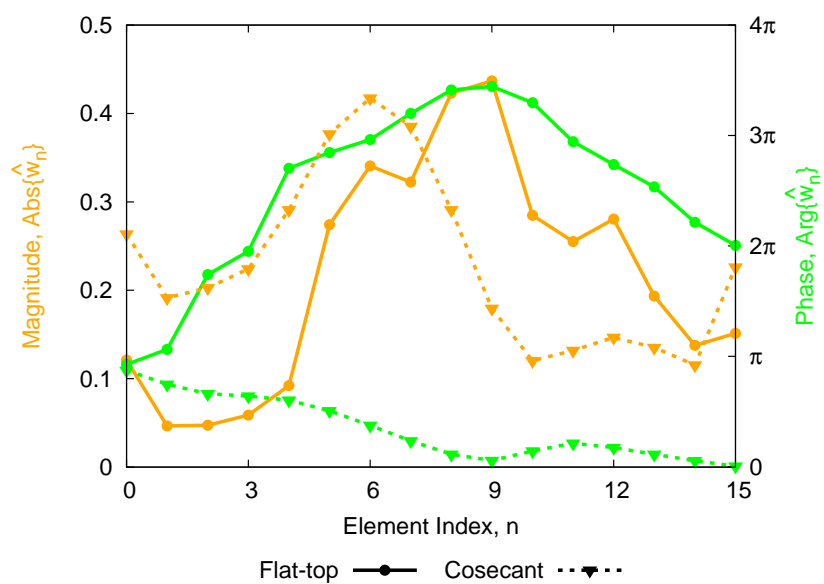


Fig. 10 - L. Tosi et *al.*, “Array Antenna Power Pattern Analysis ...”

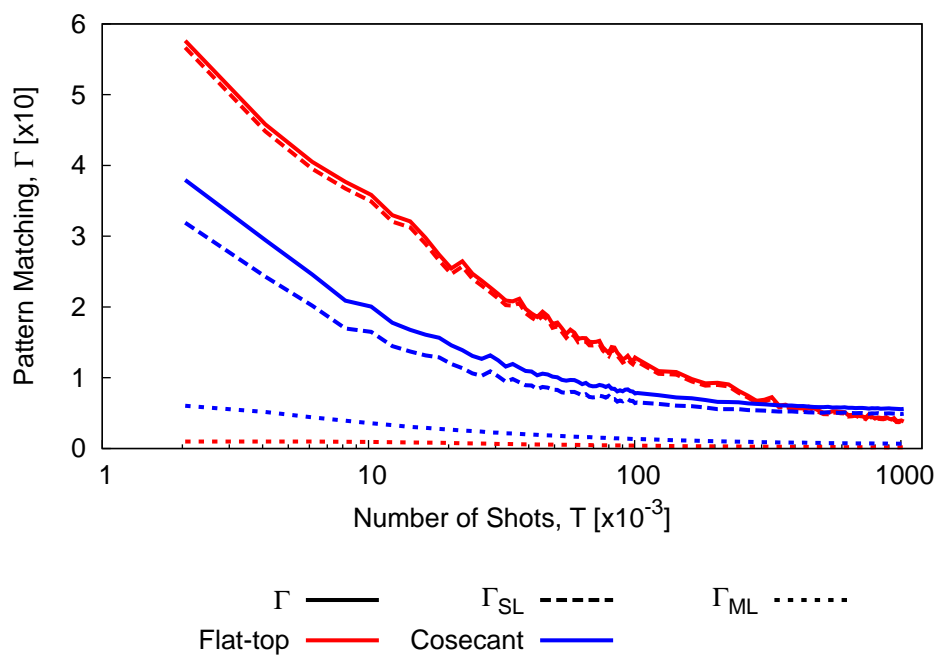
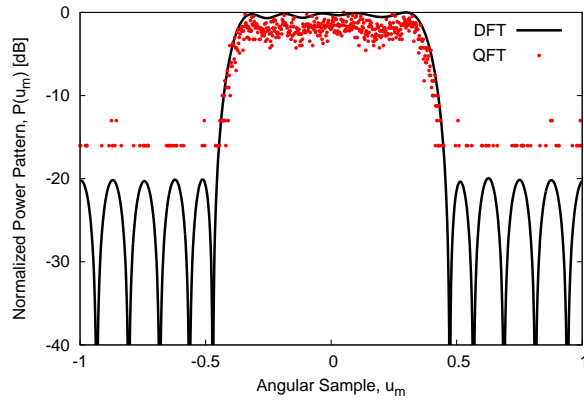
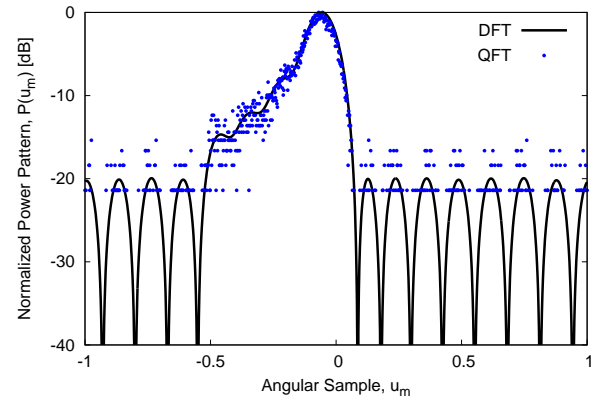


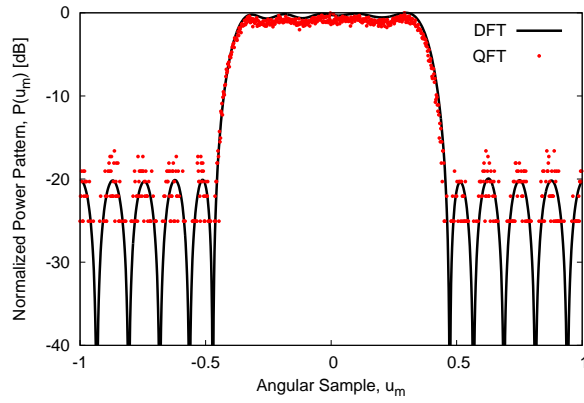
Fig. 11 - L. Tosi et *al.*, “Array Antenna Power Pattern Analysis ...”



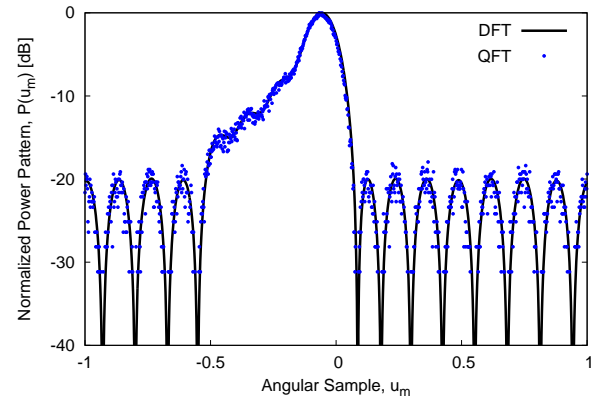
(a)



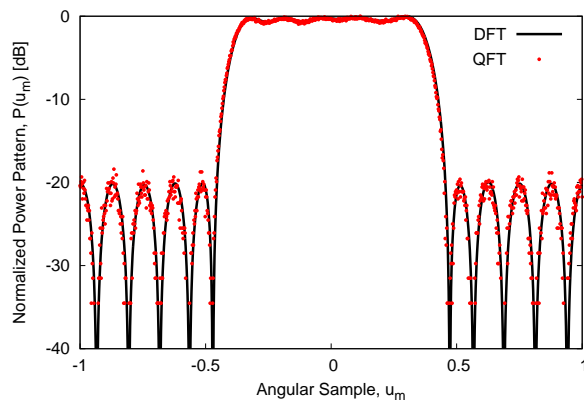
(b)



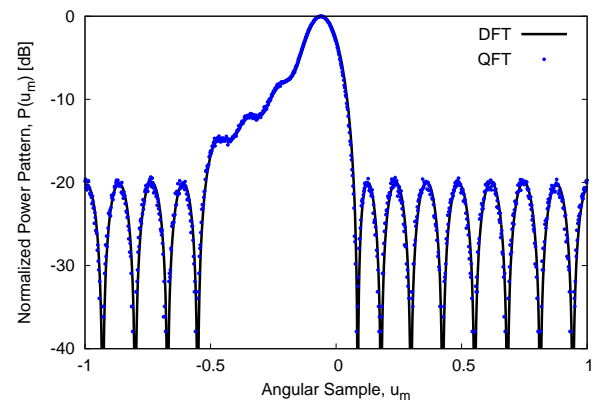
(c)



(d)



(e)



(f)

Fig. 12 - L. Tosi et al., “Array Antenna Power Pattern Analysis ...”

<i>Element Index, n</i>	<i>Normalized Excitation Module, \hat{w}_n</i>			
	<i>DC</i>			<i>Taylor</i>
	<i>SLL = -15 [dB]</i>	<i>SLL = -20 [dB]</i>	<i>SLL = -25 [dB]</i>	
0	0.4129	0.2638	0.1643	0.2971
1	0.1574	0.1535	0.1345	0.2582
2	0.1814	0.1892	0.1786	0.2161
3	0.2033	0.2232	0.2226	0.2055
4	0.2221	0.2534	0.2633	0.2270
5	0.2370	0.2780	0.2974	0.2540
6	0.2473	0.2953	0.3219	0.2653
7	0.2526	0.3043	0.3347	0.2640

Tab. I - L. Tosi et al., “Array Antenna Power Pattern Analysis ...”